The Journal of Chemical Physics

RESEARCH ARTICLE | SEPTEMBER 19 2023

Mass dipole contribution to the isotopic Soret effect in molecular mixtures

Oliver R. Gittus ; Fernando Bresme

J. Chem. Phys. 159, 114503 (2023)
https://doi.org/10.1063/5.0164253

AIP Publishing

The Journal of Chemical Physics ARTICLE pubs.aip.org/aip/jcp

Mass dipole contribution to the isotopic Soret effect in molecular mixtures

Cite as: J. Chem. Phys. 159, 114503 (2023); doi: 10.1063/5.0164253
Submitted: 21 June 2023 • Accepted: 3 August 2023 •
Published Online: 19 September 2023

Oliver R. Gittus[a] and Fernando Bresme[b]

AFFILIATIONS

Department of Chemistry, Molecular Sciences Research Hub, Imperial College London, London W12 0BZ, United Kingdom

[a]E-mail: o.gittus18@imperial.ac.uk
[b]Author to whom correspondence should be addressed: f.bresme@imperial.ac.uk

ABSTRACT

Temperature gradients induce mass separation in mixtures in a process called thermal diffusion and are quantified by the Soret coefficient S_T. Thermal diffusion in fluid mixtures has been interpreted recently in terms of the so-called (pseudo-)isotopic Soret effect but only considering the mass and moment of inertia differences of the molecules. We demonstrate that the first moment of the molecular mass distribution, the *mass dipole*, contributes significantly to the isotopic Soret effect. To probe this physical effect, we investigate fluid mixtures consisting of rigid linear molecules that differ only by the first moment of their mass distributions. We demonstrate that such mixtures have non-zero Soret coefficients in contrast with $S_T = 0$ predicted by current formulations. For the isotopic mixtures investigated in this work, the dependence of S_T on the mass dipole arises mainly through the thermal diffusion coefficient D_T. In turn, D_T is correlated with the dependence of the molecular librational modes on the mass dipole. We examine the interplay of the mass dipole and the moment of inertia in defining the isotopic Soret effect and propose empirical equations that include the mass dipole contribution.

I. INTRODUCTION

Thermal diffusion is the process by which a temperature gradient induces a concentration gradient in a mixture. It was first observed[1] in the 19th century by Ludwig and later systematically studied[2] by Soret. It was not until the 1910s, however, that thermal diffusion was "theoretically discovered," and one can speculate that it was overlooked by the original pioneers of kinetic theory because the Soret coefficient vanishes for Maxwellian molecules (point particles that repel each other with a force $F \propto r^{-5}$, where r is the inter-particle distance).[3] These equations of Enskog and Chapman already implied that components of a mixture could be separated based solely on their mass,[3] and in 1919, Chapman was the first to suggest[4] the use of thermal diffusion for separating isotopes. Isotope fractionation by thermal diffusion was first experimentally achieved in 1938 by Clusius and Dickel[5] and subsequently received considerable theoretical treatment by Furry, Jones, and Onsager, among others.[3,6]

The pseudo-isotopic Soret effect refers to the contribution to the Soret coefficient S_T from the mass and mass distribution of the particles. Using binary mixtures of isotopologues of benzene and cyclohexane, Debuschewitz and Köhler[7] demonstrated that the Soret coefficient could be split into two additive contributions,

$$S_T = S_T^{\text{chem}} + S_T^{\text{iso}}. \tag{1}$$

The chemical contribution S_T^{chem} depends on the intermolecular and intramolecular interactions (i.e., the potential energy surface), while the isotopic contribution S_T^{iso} depends only on the mass and mass distribution of the molecules. Simulations have verified that Eq. (1) holds reasonably well for binary Lennard-Jones mixtures in both the liquid and dense supercritical states even if slight couplings have been observed.[8–12] The application of Eq. (1) to the interpretation of S_T data for molecular mixtures is now standard procedure.[13–16]

To date, all models (empirical and theoretically derived) represent S_T^{iso} as a function of total masses of the particles M_i and their moments of inertia I_i. For binary mixtures,

$$S_T^{\text{iso}} = S_T^{\text{iso}}(M_1, M_2, I_1, I_2), \tag{2}$$

and for mixtures consisting of species with the same mass,

$$M_1 = M_2 = M \quad \Rightarrow \quad S_T^{\text{iso}} = S_T^{\text{iso}}(I_1, I_2; M), \tag{3}$$

where three assumptions are implicit in Eqs. (2) and (3): (1) the effect of the internal mass distribution can be modeled using only the moment of inertia; (2) rigid body moments of inertia are applicable to flexible molecules; and (3) rigid body moments of inertia $\boldsymbol{I}_i$ (3×3 matrices) can be reduced to scalars I_i. Assumptions (2) and (3) are justified for rigid linear molecules, such as diatomic molecules. Small polyatomic molecules have typically been characterized by a single principal moment of inertia $I_{i,k}$ or $I_i = 3/\sum_k I_{i,k}^{-1}$.[7,17–23] A recent study on halobenzene/*n*-alkane mixtures used $S_T^{\text{iso}}(M_1, M_2)$ because the moment of inertia is not well defined for flexible alkanes.[18] To the best of our knowledge, assumption (1) has not been tested or discussed in the literature.

How best to characterize the internal mass distribution of a molecule? The moments $\boldsymbol{\mu}_n$ of the mass distribution are a natural extension to using the total mass and moment of inertia. For a rigid body with mass density $\rho(\boldsymbol{r})$,

$$\boldsymbol{\mu}_n = \int_V \rho(\boldsymbol{r}) \boldsymbol{r}^{\otimes n} d^3\boldsymbol{r}, \tag{4}$$

where $\boldsymbol{r}^{\otimes n} = \boldsymbol{r} \otimes \boldsymbol{r} \otimes \cdots \otimes \boldsymbol{r}$ (n times) and $\otimes$ denotes the Kronecker product of two matrices. The zeroth moment $\mu_0 = M$ is the total mass of the body (scalar). The first moment $\boldsymbol{\mu}_1 = \boldsymbol{D}$ is the mass dipole (3×1 vector), which gives the center of mass when normalized by the total mass, $\boldsymbol{D}/M = \boldsymbol{r}_{\text{com}}$. The second moment $\boldsymbol{\mu}_2$ corresponds to the moment of inertia $\boldsymbol{I}$ (3×3 matrix). Higher order moments, $\boldsymbol{\mu}_{n>2}$, do not affect rigid body dynamics, and thus, the mass distribution of a rigid body can be completely represented by $\boldsymbol{\mu}_{n=0,1,2}$, i.e., by M, r_{com}, and $\boldsymbol{I}$. While M and $\boldsymbol{I}$ appear frequently in models of thermal diffusion, the impact of the mass dipole on the Soret coefficient of molecular mixtures has not been considered. Indeed, the mass dipole was introduced only very recently in the context of thermal diffusion when studying the thermal orientation (TO) and thermophoresis of anisotropic colloids.[24–26] We show here that the mass dipole is part of a more general description of the mass distribution, which adds additional contributions to the formulation summarized by Eq. (2).

In this work, we investigate the effect of the mass dipole on the Soret coefficient of isotopic mixtures of rod-like molecules. The model we employ allows for the systematic change in the moments of the mass distribution, making it possible to isolate the M, $\boldsymbol{D}$, and $\boldsymbol{I}$ contributions to the Soret coefficient. We provide a proof of principle for the mass dipole contribution in isotopic mixtures. However, the main conclusions of this work are applicable to non-isotopic mixtures as well, conveniently through Eq. (1).

II. METHODS

A. Particle model

We investigate the thermal diffusion of mixtures of rod-like molecules in which the components differ only by their internal mass distribution. Following our previous studies,[24,25] the molecules were modeled using the shish-kebab model, a rigid chain of tangent spherical monomers of effective diameter σ, of length $N = 7$.

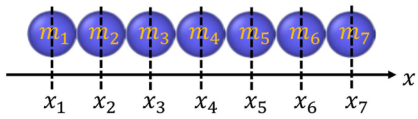

FIG. 1. The shish-kebab model of length $N = 7$.

The mass m_i of monomer i is given by a point mass at its interaction site. All intermolecular interactions were modeled using the Weeks-Chandler-Andersen (WCA)[53] potential,

$$\mathscr{V}_{\text{WCA}}(r) = \begin{cases} 4\varepsilon\left[\left(\frac{\sigma}{r}\right)^{12} - \left(\frac{\sigma}{r}\right)^{6}\right] + \varepsilon & \text{if } r \le 2^{1/6}\sigma, \\ 0 & \text{if } r > 2^{1/6}\sigma, \end{cases} \tag{5}$$

where r is the distance between two monomers and ε represents the strength of the purely repulsive pairwise interaction. These parameters, ε and σ, together with the unit of mass m are used to define the usual Lennard-Jones units, which are adopted in this work.

The total mass of each molecule was set to $M = 56m$. Noting that the total mass has been held constant, we report the reduced mass dipole $\boldsymbol{d} = \boldsymbol{D}/M$, which has a more intuitive physical meaning than $\boldsymbol{D}$: it is the displacement of the center of mass from the geometric center, $\boldsymbol{d} = d \cdot \hat{\boldsymbol{u}}_d = \boldsymbol{r}_{\text{com}} - \boldsymbol{r}_g$. The geometric center $\boldsymbol{r}_g$ was chosen as the center of symmetry of the molecule (i.e., the inversion center given the $D_{\infty h}$ point group). Since we consider freely rotating rigid bodies, their rotation is characterized by the moments of inertia I about the axes through the center of mass. The moments of mass for this model (Fig. 1) are given by (for the molecule oriented along the x axis),

$$\begin{aligned} M &= \sum_{i=1}^{7} m_i = 56m, \\ d &= \frac{1}{M}\sum_{i=1}^{7} m_i(x_i - x_g), \\ I &= \sum_{i=1}^{7} m_i(x_i - x_{\text{com}})^2, \end{aligned} \tag{6}$$

where x_i is the distance of monomer i along the molecular axis. There are no analytical solutions to Eq. (6) for a given set $\{N, M, d, I\}$ without applying additional constraints. We use numerical optimization methods to generate the mass distributions that give the desired $\{N, M, d, I\}$. Each mixture is characterized by the mass dipoles d_i and moments of inertia I_i of species $i = 1, 2$. By convention, we assign species 1 according to $I_1 > I_2$, and $d_1 > d_2$ if $I_1 = I_2$.

B. Simulation details

We performed both equilibrium and non-equilibrium molecular dynamics (NEMD) simulations of equimolar (mole fractions $x_1 = x_2 = 0.5$) binary mixtures targeting temperature $T = 3.0\ \varepsilon k_{\text{B}}^{-1}$ and pressure $P = 1.121\ \varepsilon\sigma^{-3}$, which correspond to a monomer number density of $\rho_{N,\text{mon}} = 0.398\ \sigma^{-3}$ (molecule number density $\rho_{N,m} = \rho_{N,\text{mon}}/7 = 0.0568\ \sigma^{-3}$) and volume fraction $\phi = 0.208$.

The molecules were modeled as rigid bodies; their translational and rotational degrees of freedom were integrated using the method of quaternions.[27] A timestep of $\delta t = 0.002\tau$ was used for all simulations. All simulations were performed using Large-scale Atomic/Molecular Massively Parallel Simulator (LAMMPS)[28] (v. 3 March 2020).

1. Non-equilibrium molecular dynamics simulations

Boundary-driven NEMD simulations of the mixtures were performed at an average density of $\rho_{N,\mathrm{mon}} = 0.4\sigma^{-3}$. An elongated (tetragonal) simulation cell of dimensions $(L_x, L_y, L_z) = (50, 50, 100)\sigma$ was used under 3D periodic boundary conditions. Two thermostatting regions, hot and cold, were located in the center and edges of the simulation, respectively (see Fig. 2). The thermostatting regions had a width $\Delta z = 7\sigma$ and extended over the entire (x, y) plane such that the temperature gradients were generated along the z-direction. For the thermostatting procedure, a Langevin thermostat with a time constant (damping parameter) of 1τ was applied to the hot and cold regions at temperatures T_h and T_c, respectively. The thermostat temperatures were set to $T_c = 2.5\ \varepsilon k_B^{-1}$ and $T_h = 3.5\ \varepsilon k_B^{-1}$, unless specified otherwise. The Langevin thermostats do not conserve linear momentum, so the system's center-of-mass velocity was subtracted from each particle at every timestep in order to ensure linear momentum conservation. In the stationary state, this setup results in two equal but opposite temperature gradients and therefore in equal and opposite heat fluxes such that the system is completely periodic. In order to avoid potential artifacts associated with the dynamics of the Langevin-thermostated particles,[29,30] only data pertaining to molecules with a center of geometry at a minimum distance of $(N/2)\sigma = 3.5\sigma$ from either thermostatting region were used for analysis. For each system, ten statistically independent replicas were generated, each consisting of an initial $t_e \geq 5 \times 10^4\ \tau$ to establish the stationary state followed by production runs of equal length between $10–30 \times 10^4\ \tau$. Owing to the small signal/noise ratio, it is not possible to obtain well-converged mole fraction profiles in the transient regime preceding the stationary state. The time required to reach the stationary state is of the order of the characteristic time $t_s = l^2/D$, where l is the distance between the two thermostats and D is the self-diffusion coefficient. For our NEMD simulations, t_e/t_s ~2–5, using the smaller of the two self-diffusion coefficients (corresponding to species $i = 1, 2$) for each mixture.

2. Equilibrium simulations

Equilibrium molecular dynamics (EMD) simulations of the mixtures were performed in the *NVT* ensemble. A cubic simulation cell of length $L \approx 56.05\sigma$ containing 10^4 molecules was used. The temperature was controlled by the Nosé–Hoover chain thermostat with three chains and a time constant of 10τ. Sampling consisted of 10–30 replicas for each system; each replica was equilibrated for $10^3\ \tau$ followed by $2 \times 10^4\ \tau$ of production.

Simulations of the pure fluid (same particle model but with the mass distribution given by $m_i = m$ for all monomers) in the *NPT* ensemble were performed to determine the phase coexistence diagram. These simulations used cubic cells with 3×10^4 molecules. Temperature (pressure) was controlled using a Nosé-Hoover chain thermostat (barostat) with three chains and a time constant of 1τ

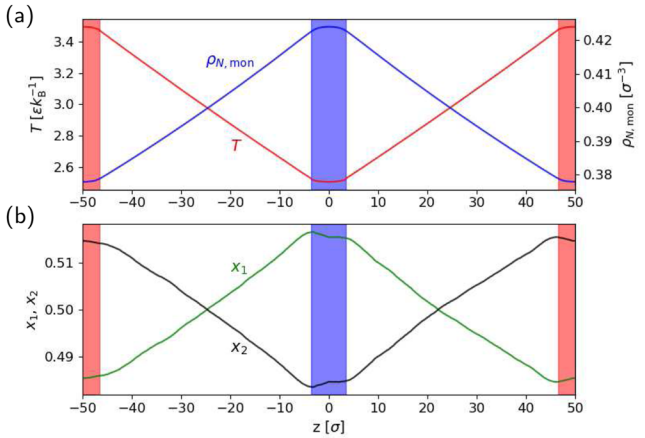

FIG. 2. Representative (a) temperature T and monomer number density $\rho_{N,\mathrm{mon}}$ profiles and (b) mole fraction, x_1 and x_2, profiles for the NEMD simulations. The blue (cold) and red (hot) indicate the location of the thermostatting regions in the simulation cell. The profiles correspond to the $(l_1 = l_2, d_1, d_2) = (80m\sigma^2, 2.7\sigma, 0)$ mixture.

(10τ). To ensure that hysteresis effects[31] were not significant, two replicas were performed for each (P, T) state point; only systems where the S_2 order parameter (see Sec. III A) of the two replicas agreed to within their statistical uncertainties were included. Along each isobar, the two replicas were generated using upward (downward) branches starting from a low-density isotropic (high-density nematic) system with gradually decreasing (increasing) temperature. Each replica consisted of 0.4–12 $\times 10^4\ \tau$ of equilibration starting from a nearby state point, followed by a $2 \times 10^4\ \tau$ production run.

C. Transport properties from simulations

The Soret coefficient S_T was evaluated from the NEMD simulations at the zero-mass-flux $(\boldsymbol{J}_1 = 0)$ stationary state as

$$S_T = -\left(\frac{1}{w_1 w_2}\frac{\nabla w_1}{\nabla T}\right)_{J_1=0} = -\left(\frac{1}{x_1 x_2}\frac{\nabla x_1}{\nabla T}\right)_{J_1=0}, \tag{7}$$

where x_i and w_i are the mole and mass fractions of component i. The local gradients ∇T and ∇x_1 were determined by fitting a straight line to their profiles within a range of $\pm 10\sigma$ around the selected state point at $T = 3.0\varepsilon k_B^{-1}$. Verification of linear response is given in the supplementary material.

The mutual diffusion coefficient D_{12} was calculated from

$$D_{12} = \frac{L_{11}}{\rho(1-w_1)T}\left(\frac{\partial \mu_{s,1}}{\partial w_1}\right)_{P,T}, \tag{8}$$

where $\mu_{s,1}$ is the specific chemical potential of component 1. For ideal mixtures,[32] such as the isotopic mixtures considered here with the same intermolecular interactions between different components,

$$\left(\frac{\partial \mu_{s,1}}{\partial w_1}\right)_{P,T} = \frac{k_B T}{w_1[M_1 - w_1(M_1 - M_2)]}. \tag{9}$$

The phenomenological coefficients L_{11} were calculated using the Green–Kubo integral formula

$$L_{11} = \frac{V}{3k_B}\lim_{t'\to\infty}\int_0^{t'}\langle \boldsymbol{J}_1(t)\cdot\boldsymbol{J}_1(0)\rangle dt, \tag{10}$$

where V is the volume of the simulation cell and the factor of 3 in the denominator averages the contributions from each spatial dimension. The mass flux is given by

$$\boldsymbol{J}_1 = \frac{1}{V}\sum_{i=1}^{N_1}\sum_{j=1}^{7} m_{j,i}\boldsymbol{v}_{j,i}, \tag{11}$$

where $\boldsymbol{v}$ is the velocity and the sums run over all seven monomers of each of the N_1 molecules of species 1. Equation (10) was evaluated from the equilibrium-*NVT* simulations using a correlation time of $t' = 500\tau$ for the upper limit of the integral, which is sufficient for well-converged integrals (see the supplementary material).

Unlike in previous studies,[33–35] the thermal diffusion coefficient D_T could not be evaluated from equilibrium simulations using the Green–Kubo approach. Owing to the rigid body constraint forces, reliable per-particle virial stress tensor-based instantaneous heat fluxes could not be obtained even when using the recently derived centroid formulation[36,37] (and using only the x component[38,39]). The formulation of instantaneous heat flux in rigid body dynamics has long been established.[40] Further work is required to implement this capability in LAMMPS. Instead, D_T was calculated from $D_T = S_T D_{12}$. This approach relies on the fact that finite-size effects associated with S_T from NEMD and D_{12} from equilibrium-*NVT* simulations are small and additionally cancel. It has recently been shown that the hydrodynamic correction of Yeh and Hummer[41] for self-diffusion coefficients can also be applied to D_{12}.[42] This correction amounts to an increase in D_{12}, D_1, and D_2 of <4% (see the supplementary material), which is smaller than the uncertainties associated with D_{12}, S_T, and therefore D_T. Regarding S_T from NEMD, extrapolating the simulation cell lengths $L_x = L_y \to \infty$ decreases S_T by ~4% (see the supplementary material). Thus, finite-size effects in S_T and D_{12} are expected to at least partially cancel when calculating D_T. This is because finite-size effects in $S_T \equiv D_T/D_{12}$ include those from D_{12}; based on our finite-size analysis of D_{12} and S_T, we expect finite-size effects of ~1% in D_T, which is smaller than its associated uncertainties. Thus, we use and report the uncorrected D_{12}, D_1, and D_2 values, which give more internally consistent values for S_T, D_{12}, and D_T. We note that using the infinite-size D_{12}, D_1, and D_2 does not change any of the qualitative trends reported in this work (see the supplementary material).

Self-diffusion coefficients were calculated using the Einstein relation. Rotational diffusion coefficients and shear viscosities were calculated from their Green–Kubo equations using an upper integration limit of 200τ and 500τ, respectively. (See the supplementary material). As with D_{12}, these transport properties were calculated from equilibrium-*NVT* simulations that use a global Nosé–Hoover chain thermostat. Global thermostats have been shown to give transport properties that are statistically indistinguishable from those of the *NVE* ensemble.[30] Especially given the weak coupling strength (large time constant), the thermostat is not expected to significantly affect the correlation functions and transport properties calculated in this work.

All statistical uncertainties reported in this work refer to the 95% confidence interval of the mean, unless stated otherwise.

III. RESULTS AND DISCUSSION

A. Equation of state and phase diagram

The simulated fluid exhibits an isotropic–nematic phase transition, and we are interested in the behavior of the mixtures in the isotropic phase. Choosing the aspect ratio of the molecules is a compromise: the maximum mass dipole achievable is determined by the length N of the shish-kebab molecule, but the nematic phase is shifted to lower volume fractions for greater aspect ratios. It is therefore necessary to map out the phase coexistence diagram to determine which thermodynamic conditions correspond to the isotropic phase.

The uniaxial orientational order parameter S_2 is zero for an isotropic fluid and unity for a perfectly aligned system. S_2 is the ensemble average of the largest positive eigenvalue P_2 of the $\boldsymbol{Q}$ tensor,

$$\boldsymbol{Q}_{\alpha\beta} = \frac{1}{N_m}\sum_{i=1}^{N_m}\left(\frac{3}{2}\hat{\boldsymbol{u}}_{i,\alpha}\hat{\boldsymbol{u}}_{i,\beta} - \frac{1}{2}\delta_{\alpha\beta}\right), \quad \alpha,\beta = x,y,z, \tag{12}$$

$$S_2 = \langle P_2(\boldsymbol{n}\cdot\hat{\boldsymbol{u}})\rangle = \langle P_2(\cos\theta_n)\rangle = \frac{3}{2}\langle\cos\theta_n\rangle - \frac{1}{2}, \tag{13}$$

where the director $\boldsymbol{n}$ is the eigenvector associated with P_2 and $\hat{\boldsymbol{u}} = \hat{\boldsymbol{u}}_d$ is the unit vector along the long molecular axis. Numerical data for the estimated isotropic–nematic coexistence temperatures and upper/lower bounds on the coexistence densities are given in the supplementary material.

The phase diagram of the pure fluid is shown in Fig. 3. In classical systems, ensemble averages over thermodynamic observables are independent of the mass and mass distribution of the particles, and

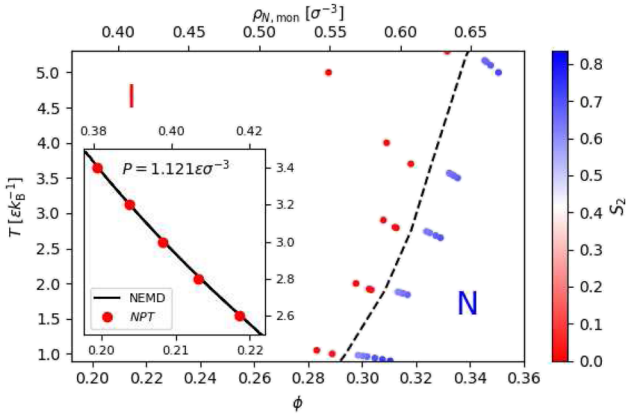

FIG. 3. Phase diagram and equation of state (EOS). T, $\rho_{N,\mathrm{mon}}$, and ϕ are the temperature, monomer number density, and volume fraction, respectively. The data are color coded according to the uniaxial (orientational) order parameter S_2. The dashed isotropic–nematic coexistence line is to guide the eye. The inset shows the EOS at pressure $P = 1.121\varepsilon\sigma^{-3}$, as predicted by equilibrium-*NPT* and NEMD simulations. Symbols: *I* = isotropic and *N* = nematic.

the phase diagram is therefore applicable to the isotopic mixtures under equilibrium conditions. All the NEMD simulations correspond to thermodynamic conditions, $T \geq 2.0\,\varepsilon k_B^{-1}$ and $\phi < 0.24$, that are safely within the isotropic region of the phase diagram. Each set of NEMD profiles corresponds to the equation of state (EOS) at the simulated pressure, as defined by the component (P_{zz}) parallel to the heat flux vector. The inset of Fig. 3 shows that NEMD simulations reproduce the equilibrium EOS at $P = 1.121\varepsilon\sigma^{-3}$ and therefore that local equilibrium is fulfilled.

B. Mass dipole contribution and its microscopic origin

In this section, we consider mixtures with $I = I_1 = I_2$ but $d_1 \neq d_2$ for which all current models of thermal diffusion predict $S_T = 0$ (see, e.g., the reviews Refs. 13–16 and 43 and the references contained therein). Figures 4(a-i) and 4(b-i) contains the main result of this work: mixtures with components that differ only by their mass dipole have non-zero Soret coefficients. Indeed, the mole fraction profiles for one such mixture are shown in Fig. 2, providing clear evidence for species separation in the thermal field. In all

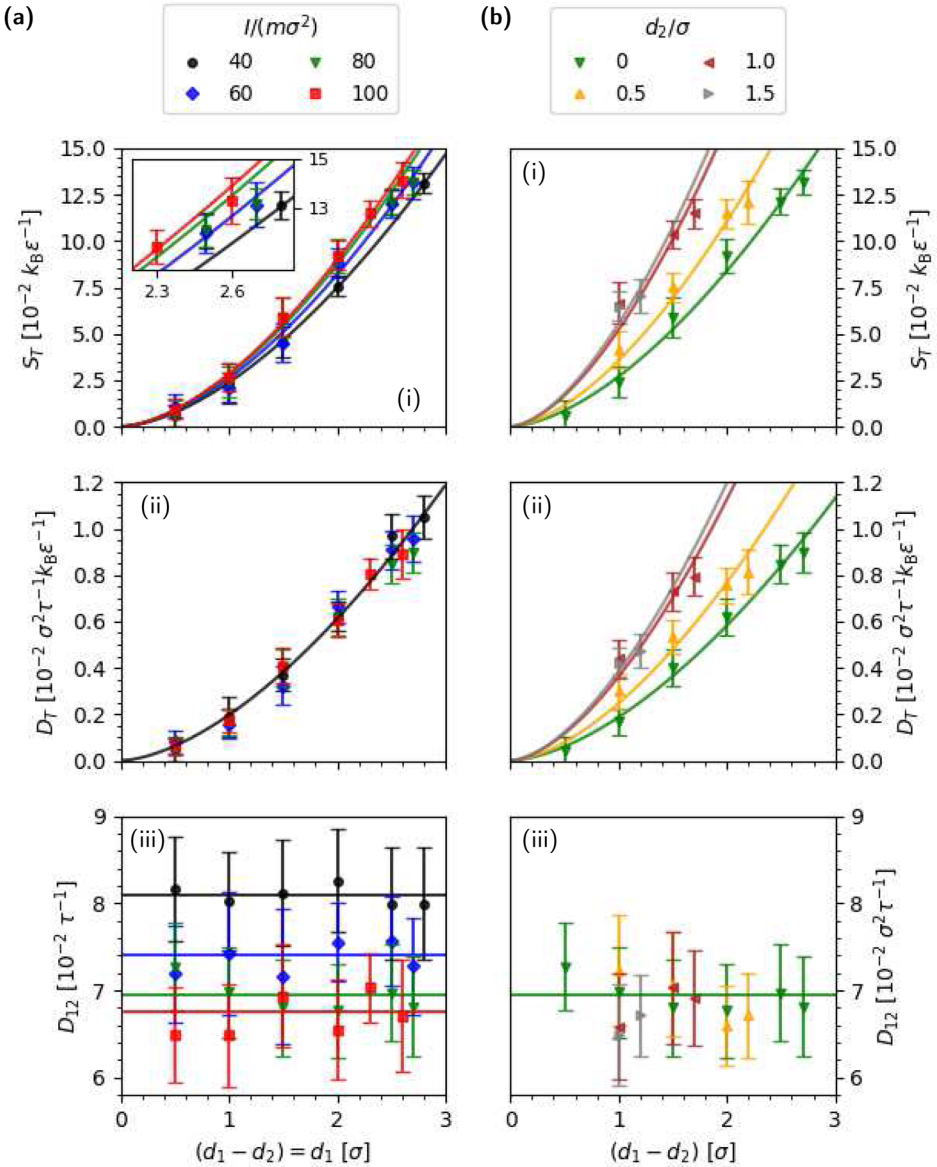

FIG. 4. Transport coefficients for the isotopic mixtures with (a) $I = I_1 = I_2$ and $d_2 = 0$ and (b) $I = I_1 = I_2 = 80m\sigma^2$ and $d_1 \neq d_2$. The (i) Soret coefficient S_T, (ii) thermal diffusion coefficient D_T, and (iii) mutual diffusion coefficient D_{12} as a function of $d_1 - d_2$. d_i and I_i are the mass dipole and moment of inertia of species $i = 1, 2$. The solid lines show equations that model the data: see the main text for details.

cases, $S_T > 0$, which indicates that the species with the greater mass dipole is thermophobic and preferentially collects in the cold region. Assigning an interaction strength typical of simple molecular fluids, $\varepsilon/k_B = 10^2$ K, gives $S_T = 1\text{–}15 \times 10^{-3}$ K^{-1} at $T = 300$ K ($T = 3.0\,\varepsilon k_B^{-1}$) for the mass dipole contribution [Figs. 4(a-i) and 4(b-i)]. This is of comparable magnitude to the entire (pseudo-)isotopic Soret effect in many molecular mixtures.[7,17,18]

We probe the phenomenology of $S_T \equiv D_T/D_{12}$ by considering the thermal diffusion coefficient D_T and mutual diffusion coefficient D_{12}. As shown in Fig. 4(a-iii), D_{12} decreases with increasing I for mixtures with $I = I_1 = I_2$ and $d_2 = 0$ but is essentially constant with d_1. Furthermore, the constant value of D_{12} determined by fitting to the $D_{12}(d_1;\ I = 80m\sigma^2, d_2 = 0)$ data accurately predicts the D_{12} values for mixtures with $d_2 \neq 0$ as well [Fig. 4(b-iii)], indicating that D_{12} does not significantly depend on either mass dipole, d_1 or d_2, at least relative to the statistical uncertainties associated with the data.

With regard to D_T, all the data for the $I = I_1 = I_2$ and $d_2 = 0$ mixtures can be accurately described by a power law dependence $D_T = a(d_1 - d_2)^k$ [Fig. 4(a-ii)], indicating that D_T is only weakly dependent on the moment of inertia. The exponent $k = k_{d_2=0} = 1.6 \pm 0.1$ was determined by fitting the equation $\ln D_T = k \ln(d_1 - d_2) + \ln a$ to the $d_2 = 0$ data (see the supplementary material). Considering mixtures with $d_2 \neq 0$, fits to the equation $D_T = a(d_1 - d_2)^{k_{d_2=0}}$ accurately reproduces the simulation data [Fig. 4(b-ii)]. Thus, the effect of changing d_2 while keeping $d_1 - d_2$ constant can be captured by the prefactor a, which increases with increasing d_2, as shown explicitly in the inset of Fig. 8(b) in the supplementary material.

Finally, we return to S_T, which we predict with the equation

$$S_T[d_1, d_2, I = I_1 = I_2] = \frac{D_T[d_1, d_2]}{D_{12}[I]} = \frac{a(d_1 - d_2)^k}{c_I[I]}, \qquad (14)$$

where $k = k_{d_2=0}$ describes the whole dataset and a and c_I were determined by the fits to D_T and D_{12}, respectively. We show in Figs. 4(a-i) and 4(b-i) that Eq. (14) accurately predicts S_T and captures its weak dependence on I, which can be discerned for large values of $d_1 - d_2$, as shown in the inset of Fig. 4(a-i).

We additionally calculate D_{12} using the Darken approximation $D_{MS} \approx D_{MS}^{Darken} = x_2 D_1 + x_1 D_2$, where D_{MS} is the Maxwell–Stefan

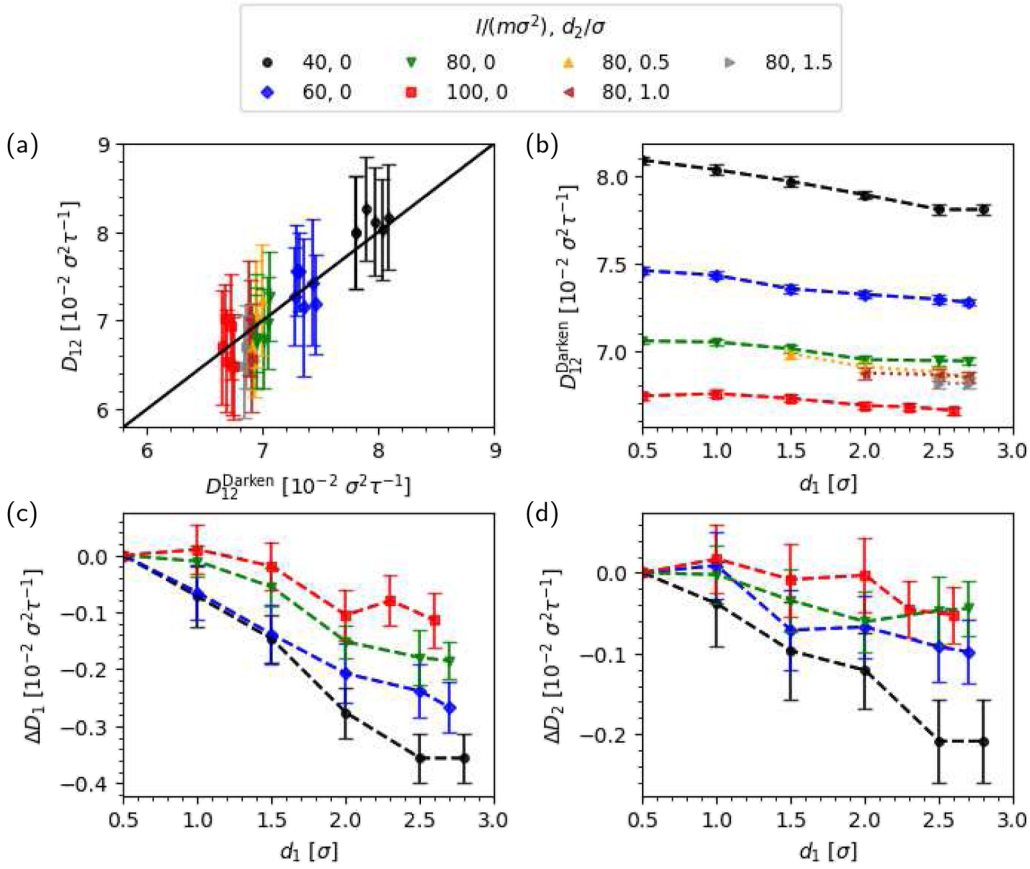

FIG. 5. (a) The mutual diffusion coefficient D_{12} vs the Darken approximation D_{12}^{Darken}. (b) D_{12}^{Darken}, (c) ΔD_1, and (d) ΔD_2 as a function of the mass dipole, d_1, of species 1. $\Delta D_i = D_i - D_i(d_1 = 0.5\sigma)$ is the change in self-diffusion coefficient D_i of species $i = 1, 2$ relative to the corresponding mixture with $d_1 = 0.5\sigma$.

diffusion coefficient related to the Fickian D_{12} via $D_{12} = \Gamma D_{\mathrm{MS}}$, where Γ is the thermodynamic factor ($\Gamma = 1$ for the ideal mixtures considered here). The Darken approximation D_{12}^{Darken} predicts values in excellent agreement with the (non-approximate) D_{12} values [Fig. 5(a)], indicating that displacement cross correlations between particles do not play an important role in determining D_{12}. Thus, the behavior of D_{12} can be rationalized in terms of the self-diffusion coefficients D_1 and D_2. As shown in Fig. 5(b), D_{12}^{Darken} features a weak but discernible dependence on d_1 (and therefore $d_1 - d_2$), which was masked by the greater uncertainties associated with D_{12} calculated from the Green–Kubo integral formula. D_1 and D_2 also depend weakly on the mass dipole d_1 [Figs. 5(c) and 5(d)]. Unsurprisingly, the impact of d_1 on D_1 is greater than on D_2 with $\Delta D_1/\Delta D_2 \sim 1$–4, where $\Delta D_i = D_i(d_1) - D_i(d_1 = 0.5\sigma)$. Thus, the weak dependence of D_{12} on the mass dipoles d_1 and d_2 can be primarily attributed to the effect of d_i on D_i. (See the supplementary material for additional data on the diffusion coefficients and related quantities).

The mass dipole also affects the rotational diffusion of the rod-like molecules. We show in Fig. 6(a) that the rotational diffusion coefficient $D_{r,1}$ decreases with increasing mass dipole d_1. $D_{r,i}$ is the rotational diffusion coefficient of species $i = 1, 2$. The rotational diffusion coefficient decreases with increasing moment of inertia, as expected. The translational and rotational diffusion coefficients are coupled with $15 > (D_i/D_{r,i})/(\sigma^2\,\mathrm{rad}^{-2}) > 13$ for all the mixtures considered in this section. As shown in Fig. 6(b), the ratio $D_1/D_{r,1}$ increases with the mass dipole d_1 but is statistically independent of I within the statistical uncertainties of our data. We note that comparing to previous simulations[44] of systems of the same WCA shish-kebab model but at the different temperature $T = 1\ \varepsilon k_{\mathrm{B}}^{-1}$, the ($N = 7$, $\rho_{N,m} = 0.0568\ \sigma^{-3}$) state point studied in this work is expected to be in the semidilute regime, where the translational and rotational diffusion are known to be coupled.[45]

We conclude from Fig. 4 that the Soret coefficient depends on the mass dipoles mainly through D_T. We show in Figs. 6(c) and 6(d) that D_T is positively correlated with the differences in rotational diffusion coefficients, $-(D_{r,1} - D_{r,2})$, and translational diffusion coefficients, $-(D_1 - D_2)$. We expect the rotational correlation reflects librational modes that influence the thermal transport and therefore D_T.

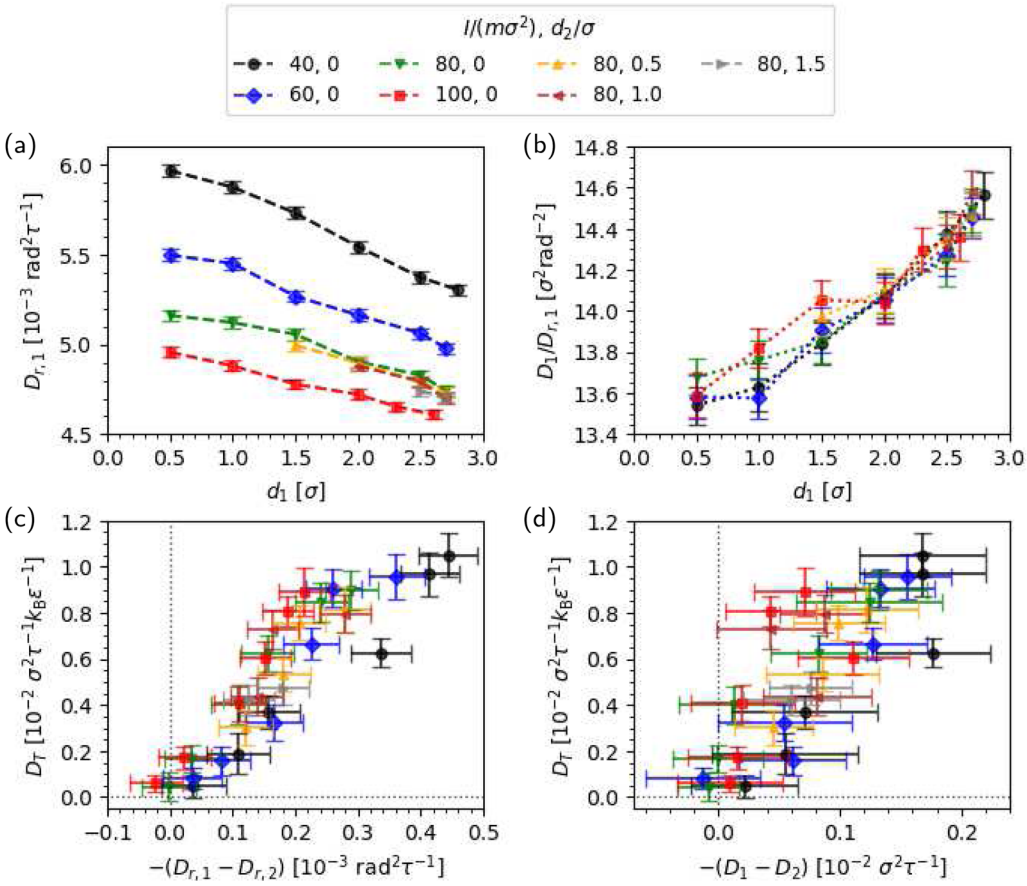

FIG. 6. Rotational and translational diffusion coefficients and their correlation with the thermal diffusion coefficient D_T. (a) $D_{r,1}$ as a function of the mass dipole d_1 of species 1. (b) The ratio $D_1/D_{r,1}$ as a function of d_1. (c) D_T vs $-(D_{r,1} - D_{r,2})$. (d) D_T vs $-(D_1 - D_2)$. $D_{r,i}$ and D_i are the rotational and translational diffusion coefficients, respectively, of species $i = 1, 2$.

Hence, to probe the microscopic mechanism associated with librational modes and its dependence on the molecular internal degrees of freedom, we calculate the power spectra of various velocity autocorrelation functions (VACFs). We consider the "all-atom" VACF, C_{atom}, as well as the rotational and translational center-of-mass VACFs of the rigid molecules, C_{rot} and C_{trans}, respectively,

$$C_{\text{atom}}(t) = \frac{\langle \boldsymbol{v}_i(t) \cdot \boldsymbol{v}_i(0) \rangle}{\langle v_i^2(0) \rangle}, \tag{15}$$

$$C_{\text{rot}}(t) = \frac{\langle \boldsymbol{\omega}_j(t) \cdot \boldsymbol{\omega}_j(0) \rangle}{\langle \omega_j^2(0) \rangle}, \tag{16}$$

$$C_{\text{trans}}(t) = \frac{\langle \boldsymbol{v}_{\text{COM},j}(t) \cdot \boldsymbol{v}_{\text{COM},j}(0) \rangle}{\langle v_{\text{COM},j}^2(0) \rangle}, \tag{17}$$

where $\boldsymbol{v}_i$ is the velocity of monomer i, $\boldsymbol{\omega}_j$ is the angular velocity of rigid molecule j, $v_{\text{COM},j}$ is the center-of-mass velocity of rigid molecule j, and t is the elapsed time from an arbitrary starting time. The power spectrum is then given by the Fourier transform of the corresponding VACF,

$$I_X(\nu) = \lim_{t' \to \infty} \int_{-t'}^{t'} C_X(t) e^{-i2\pi\nu t} dt, \tag{18}$$

where I_X is the intensity and ν is the frequency.

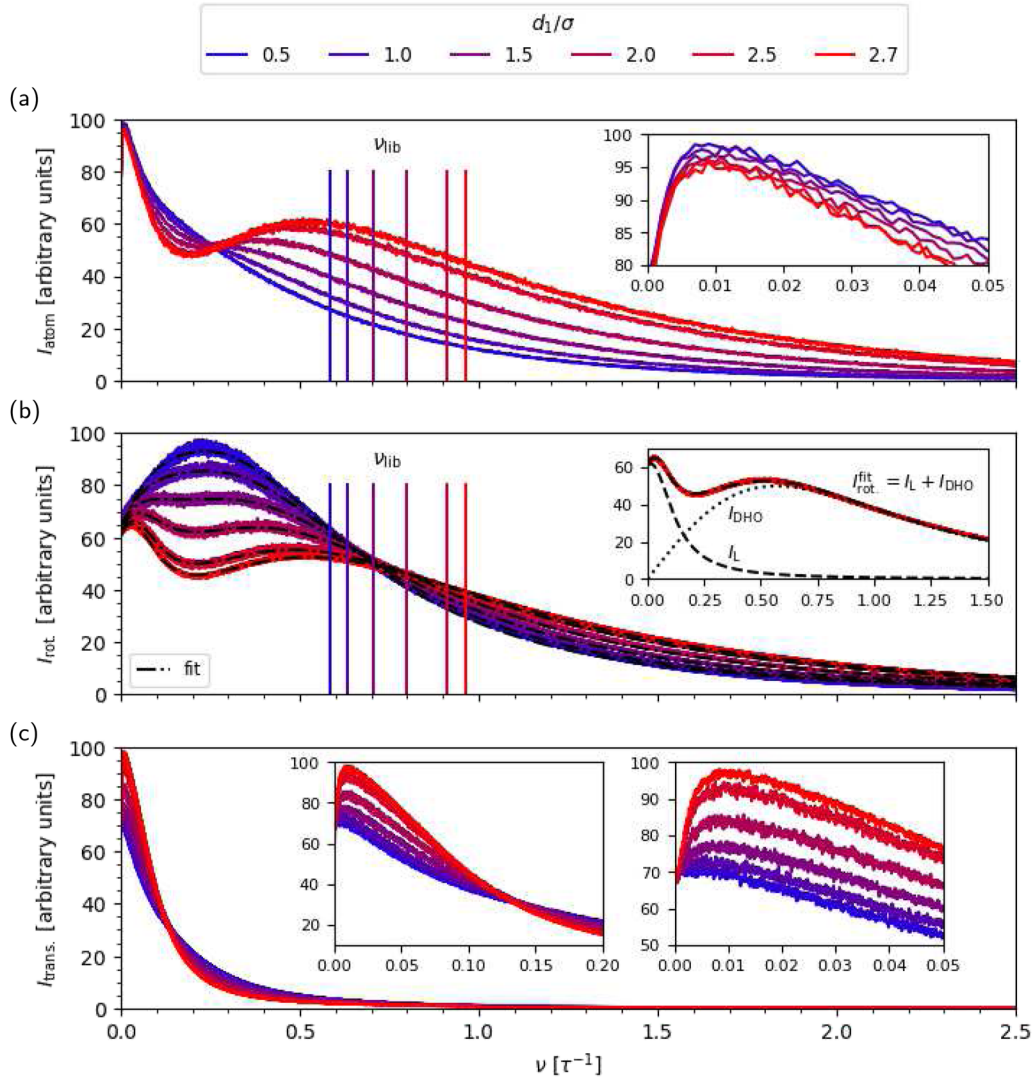

FIG. 7. Power spectra of species 1 of the $(l_1 = l_2, d_1, d_2) = (80m\sigma^2, d_1, 0)$ mixtures. The intensity I_X vs frequency ν for the (a) "all-atom" (I_{atom}) (b) rotational (I_{rot}) and (c) translational center-of-mass (I_{trans}) power spectra. In (a) and (b), the vertical solid lines show the librational mode frequencies ν_{lib}. In (b), the dashed-dotted (-.) lines denote the fitted spectra I_{fit} and the inset shows the individual fitted functions for the $(l_1 = l_2, d_1, d_2) = (80m\sigma^2, 2.7\sigma, 0)$ mixture.

The power spectra of species 1 in the $I = I_1 = I_2 = 80m\sigma^2$ and $d_2 = 0$ mixtures are shown in Fig. 7. For large mass dipoles, I_{atom} features a peak at $\sim 0.5\tau^{-1}$ indicative of a librational mode. Increasing the mass dipole increases the frequency of the librational mode. This librational mode is also reflected in I_{rot}. For low mass dipoles, a single peak is observed at ~ 0.2–$0.3\tau^{-1}$, which contains contributions from both the libration and a lower frequency mode. Upon increasing d, the librational mode is blue-shifted and two distinct peaks are observed.

In order to disentangle contributions from the different modes, we fit the rotational power spectra I_{rot} using the following equations:

$$I_{fit} = I_L + I_{DHO}, \tag{19}$$

$$I_L = \frac{a_L}{1 + \left(\frac{\nu - \nu_L}{c_L}\right)^2}, \tag{20}$$

$$I_{DHO} = \frac{D\gamma}{(\nu_0^2 - \nu^2)^2 + \gamma^2\nu^2}, \tag{21}$$

where the Lorentzian-like function I_L captures the low frequency peak at $\nu \sim 10^{-2}\tau^{-1}$. In spectroscopy, librations are typically modeled as damped harmonic oscillators (DHO). In Eq. (21) for the DHO, D is the oscillator intensity constant, γ is the damping constant, and ν_0 is its frequency (band position). Using the $I = I_1 = I_2 = 80m\sigma^2$ and $d_2 = 0$ mixtures as an example, we show in Fig. 7(b) that fitting Eq. (19) accurately reproduces I_{rot}. Extracting the librational frequencies $\nu_{lib} = \nu_0$ from the fits, it is evident that ν_{lib} increases with d_1 (Fig. 7).

In Fig. 8, we show that D_T is highly correlated with the difference in librational frequencies of species 1 ($\nu_{lib,1}$) and species 2 ($\nu_{lib,2}$). The effect of the mass dipole on ν_{lib} can be large; we observe $\nu_{lib,1} - \nu_{lib,2}$ values of up to ~100% of $\nu_{lib,2}$. We fit the data to the equation $D_T = b(\nu_{lib,1} - \nu_{lib,2})$, demonstrating a direct proportionality relationship with D_T. Given their statistical uncertainties, all data points agree with the fitting except for the $(I_1 = I_2, d_1, d_2) = (40m\sigma^2, 2.8\sigma, 0)$ mixture, which corresponds to the greatest $\nu_{lib,1} - \nu_{lib,2}$ value of all the mixtures considered in this section. This suggests that D_T may saturate at sufficiently large $\nu_{lib,1} - \nu_{lib,2}$ values, beginning from $\sim 0.5\tau^{-1}$. We conclude that the librational frequency is sensitive to the mass dipole and that the mass dipole contribution to D_T is highly correlated with the modification of the librational mode and therefore the short-time dynamics of the rod-like molecules.

C. Coupling with the moment of inertia contribution

In this section, we examine how the mass dipoles affect the Soret coefficient of mixtures with non-zero moment of inertia contributions. We consider mixtures with components that differ only in their moments of inertia ($I_1 \neq I_2, d_1 = d_2$) with $I_1, I_2 = 10$–$270m\sigma^2$ and ratios $I_1/I_2 = 1$–27 and then mixtures with $I_1 \neq I_2$ and $d_1 \neq d_2$.

First we consider the simplest case of mass-symmetric molecules: $I_1 \neq I_2$ and $d_1 = d_2 = 0$. The Soret coefficients for these mixtures are shown in Figs. 9(a) and 9(b). In all cases $S_T > 0$, indicating that the component with the greater moment of inertia (species 1) is thermophobic. For molecular mixtures, the pseudo-isotopic Soret effect is usually modeled by the empirical equation

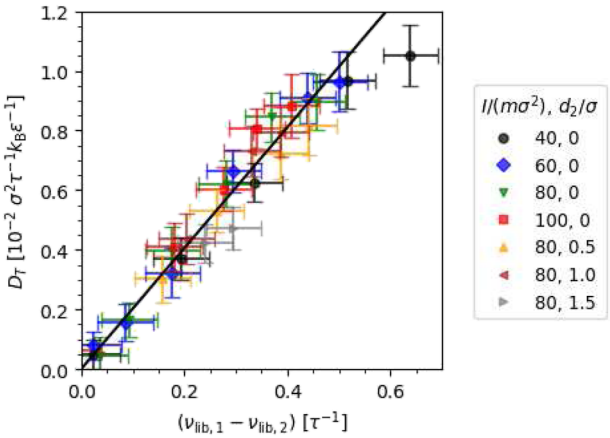

FIG. 8. Thermal diffusion coefficient D_T as a function of $\nu_{lib,1} - \nu_{lib,2}$, where $\nu_{lib,i}$ is the librational frequency of species i. The solid line shows the fit to $D_T = b(\nu_{lib,1} - \nu_{lib,2})$. Error bars correspond to maximum/minimum values based on the sensitivity of the fitting procedure for Eqs. (19)–(21).

$$S_T = S_T^{chem} + S_T^{iso} = S_T^{chem} + a_M\frac{M_1 - M_2}{M_1 + M_2} + b_I\frac{I_1 - I_2}{I_1 + I_2}, \tag{22}$$

where S_T^{iso} was originally taken by analogy to the description of gaseous mixtures[3,19,46] and adjusted for liquids by the prefactors a_M and b_I.[13,20] For the mixtures considered here, Eq. (22) reduces to

$$S_T = b_I\frac{I_1 - I_2}{I_1 + I_2}, \tag{23}$$

which is also retrieved from the theoretical model[47] of Villain-Guillot and Würger (derived by considering velocity fluctuations in a hard-bead model with elastic collisions) when setting $M_1 = M_2$. As shown in Fig. 9(a), Eq. (23) is in relatively good agreement with our simulation results. However, it is unable to predict all data points within their associated uncertainties. Previous simulations of binary isotopic mixtures of Lennard-Jones dumbbells with $I_1/I_2 = 1$–40 have shown very good agreement with the moment of inertia contribution given by Eq. (23).[8,12] These simulations did not account for the mass dipole, but this contribution is likely to be small with $d_1 - d_2 \leq 1\sigma$ for the dumbbells. More generally, Eq. (22) has been able to accurately model the experimental Soret coefficients of relatively low molecular mass non-polar mixtures[7] and isotope mixtures.[7,19–23] However, $M_1 + M_2$ and $I_1 + I_2$ in these mixtures were almost constant; the terms in Eq. (22) could also be written in terms of absolute differences $M_1 - M_2$ and $I_1 - I_2$. Indeed, Wittko and Köhler found that the isotopic substitution C_6H_{12} to C_6D_{12} results in a constant shift in S_T, irrespective of the nature of the other component.[17] This trend is not reproduced by Eq. (22). Thus, we also fit our simulation data to

$$S_T = b_I(I_1 - I_2), \tag{24}$$

which similarly reproduces the S_T values relatively well, as shown in Fig. 9(b).

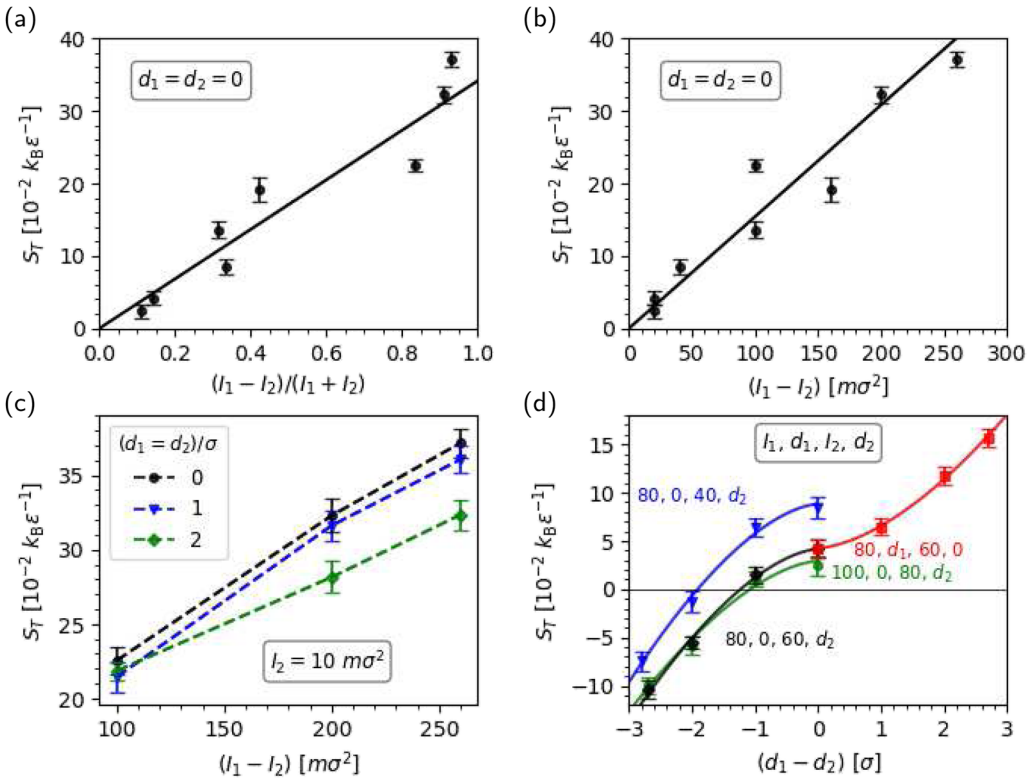

FIG. 9. The Soret coefficient S_T as a function of (a) the relative $(I_1 - I_2)/(I_1 + I_2)$ and (b) absolute $(I_1 - I_2)$ differences in moment of inertia I_i of species $i = 1, 2$ for mixtures with mass dipoles $d_1 = d_2 = 0$; (c) $(I_1 - I_2)$ for mixtures with $d_1 = d_2$; and (d) $(d_1 - d_2)$ for mixtures with (I_1, d_1, I_2, d_2). In (d), the solid lines show fits to Eq. (25), and the label units for I_i and d_i are $m\sigma^2$ and σ, respectively.

We emphasize that Eqs. (23) and (24) are empirical equations, and how accurately they model the moment of inertia contribution must be considered on a case-by-case basis for each mixture. Additionally, b_I is typically fit simultaneously with multiple other coefficients,[7,17] making it difficult to isolate the moment of inertia term. Isotopic substitution changes both the mass and inertia of a molecule. Thus, even for isotopic mixtures, the moment of inertia must be considered together with the total mass (and the mass dipole). Only recently, in simulations of isotopic mixtures of Lennard-Jones dumbbells with $M_1 = M_2$, has the moment of inertia contribution been studied independently from total mass contribution.[12] The shish-kebab model used in this work allows us to isolate the moment of inertia contribution from both the total mass and mass dipole contributions.

Next, we consider mixtures with $I_1 \neq I_2$ and $d_1 = d_2 \neq 0$. As shown in Fig. 9(c), increasing $d_1 = d_2$ while holding I_1 and $I_2 = 10m\sigma^2$ constant decreases S_T, and this decrease is more pronounced when I_1 (i.e., $I_1 - I_2$) and S_T are larger. In terms of its relative magnitude, S_T decreases by ~15% when increasing $d_1 = d_2$ from 0 to 2σ for the entire $100 \leq (I_1 - I_2)/(m\sigma^2) \leq 260$ range (15% is comparable to the uncertainties for $I_1 - I_2 = 100m\sigma^2$). This demonstrates that the moment of inertia contribution is coupled with the mass dipole even when $d_1 = d_2$.

Finally, we consider mixtures with $I_1 \neq I_2$ and $d_1 \neq d_2$. As shown in Fig. 9(d), S_T can be tuned by the mass dipoles d_1 and d_2 when holding I_1 and I_2 constant. In all cases, S_T increases with $d_1 - d_2$, and the mass dipole contribution can both enhance or compete with the moment of inertia contribution. All current models of thermal diffusion predict that when the components differ by only their internal mass distribution, the component with the greater moment of inertia is thermophobic ($S_T > 0$). Crucially, we demonstrate that by increasing $-(d_1 - d_2)$, the competing mass dipole contribution causes a reversal in sign of S_T and species 1 ($I_1 > I_2$) becomes thermophilic ($S_T < 0$), or can lead to the inhibition of thermal diffusion ($S_T = 0$).

Following from the power law dependence of the mass dipole contribution [Eq. (14)] described in Sec. III B, we model the $I_1 \neq I_2$ and $d_1 \neq d_2$ mixtures using the equation

$$S_T = a(d_1 - d_2)|d_1 - d_2|^{k-1} + c_I, \tag{25}$$

where $k = k_{d_2=0} = 1.6 \pm 0.1$ as determined in Sec. III B. The prefactor a accounts for the strength of the mass dipole contribution including the coupling with the moments of inertia, while the constant $c_I(I_1, I_2)$ represents only the inertia contribution. As shown

in Fig. 9(d), Eq. (25) is in excellent agreement with our simulation data; all data points agree to within their statistical uncertainties. a depends on both I_1 and I_2, indicating that the mass dipole contribution is coupled with the moments of inertia.

D. An empirical equation for the isotopic Soret effect

In this section, we propose an empirical equation for the isotopic Soret effect that includes the mass dipole contribution. Building on the success of equations of the form $S_T^{\text{iso}} = S_T^M(M_1, M_2) + S_T^I(I_1, I_2)$ for modeling experimental[7,17,19–23,48] and simulation[8] data, we assume that contributions from the different moments of the mass distribution are only weakly coupled and seek an equation of the form

$$S_T^{\text{iso}}(M_1, M_2, d_1, d_2, I_1, I_2) = S_T^M(M_1, M_2) + S_T^d(d_1, d_2) + S_T^I(I_1, I_2). \tag{26}$$

All mixtures considered in this work correspond to $M_1 = M_2$ and thus $S_T^M = 0$. However, we note that $S_T^M \propto (M_1 - M_2)/(M_1 + M_2)$, $S_T^M \propto (M_1 - M_2)$, and $S_T^M \propto -(M_1^{-1} - M_2^{-1})$ have been used to model a range of molecular mixtures.[7,17,18,48] For S_T^d, we propose

$$S_T^d(d_1, d_2) = (a_1 d_s + a_2)(d_1 - d_2)|d_1 - d_2|^{k-1}, \tag{27}$$

where $d_s = \min\{d_1, d_2\}$ is the smaller mass dipole, a_1 and a_2 are constants, and $k = k_{d_2=0} = 1.6 \pm 0.1$ as determined in Sec. III B. The $(a_1 d_s + a_2)$ term stems from the observation that a in Eq. (14) is approximately linear with d_s ($d_2 = d_s$ for the $I_1 = I_2$ mixtures considered in Sec. III B), as evident from the inset of Fig. 8(b) in the supplementary material. For S_T^I, we test both Eq. (23) (model A) and Eq. (24) (model B). Thus, for the isotopic mixtures studied in this work, the empirical equations are model A,

$$S_T^{\text{A}} = S_T^d(d_1, d_2) + b_I \frac{I_1 - I_2}{I_1 + I_2}, \tag{28}$$

and model B,

$$S_T^{\text{B}} = S_T^d(d_1, d_2) + b_I(I_1 - I_2). \tag{29}$$

For the mass dipole contribution S_T^d, the parameters a_1 and a_2 were fit using only the $I_1 = I_2$ mixtures. Analogously, for the moment of inertia contribution S_T^I, the parameters b_I were fit using only the

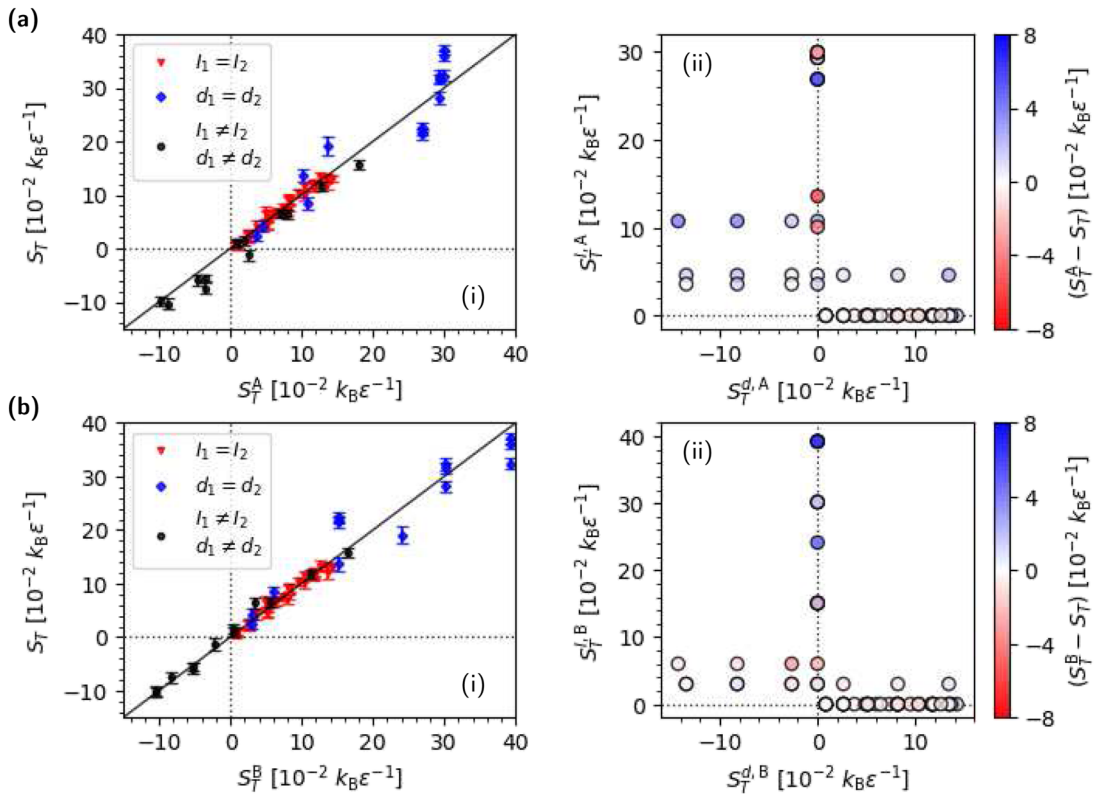

FIG. 10. Empirical models (a) A [Eq. (28)] and (b) B [Eq. (29)] for the isotopic Soret effect. (i) S_T vs S_T^{X} for model X = A, B, where S_T^{X} and S_T are the predicted and reference (simulated) Soret coefficients, respectively. (ii) The error $S_T^{\text{X}} - S_T$ as a function of the mass dipole contribution $S_T^{d,\text{X}}$ and moment of inertia contribution $S_T^{I,\text{X}}$ of model X = A, B. Data are color coded according to the error $S_T^{\text{X}} - S_T$.

$d_1 = d_2$ mixtures. The $(I_1 \neq I_2, d_1 \neq d_2)$ mixtures were not used in the fitting procedure, and $S_T^{X=A,B}$ values for these mixtures are therefore true predictions.

We show in Fig. 10 that both models are in relatively good agreement with our simulation data. For the $d_1 = d_2$ mixtures, $S_T^X = S_T^I$ have *maximum* absolute errors (MAEs) of $7.2 \times 10^{-2}\ k_B\varepsilon^{-1}$ and $7.6 \times 10^{-2}\ k_B\varepsilon^{-1}$ for models A and B, respectively. These are ~4 times greater than the MAE of $1.8 \times 10^{-2}\ k_B\varepsilon^{-1}$ for the $I_1 = I_2$ mixtures for which $S_T^X = S_T^d$. Thus, Eqs. (28) and (29) more accurately model the mass dipole contribution compared to the moment of inertia contribution. For the $(I_1 \neq I_2, d_1 \neq d_2)$ mixtures, models A and B have MAEs of $4.0 \times 10^{-2}\ k_B\varepsilon^{-1}$ and $3.0 \times 10^{-2}\ k_B\varepsilon^{-1}$, respectively. We note that while a full range of mass dipoles ($d_i \lesssim 3$ for this particle model) has been explored, the simulated $(I_1 \neq I_2, d_1 \neq d_2)$ mixtures correspond to a more limited range of moments of inertia [see Fig. 9(d)]. Using the same range of (I_1, I_2) as the $d_1 = d_2$ mixtures would presumably result in higher MAEs for the $(I_1 \neq I_2, d_1 \neq d_2)$ mixtures. For the mixtures studied in this work, the accuracy of the empirical models is limited by the (in)accuracy of the S_T^I term rather than the assumption that the moments of the mass distribution are uncoupled.

Next, we consider the validity of the weak coupling approximation. As shown in Fig. 4(a-iii), D_{12} increases (S_T decreases) by ~20% when decreasing $I = I_1 = I_2$ from $100m\sigma^2$ to $40m\sigma^2$, which corresponds to the largest change in the mass dipole contribution due to the coupling with the moments of inertia. The a_1 and a_2 coefficients in S_T^d [Eq. (27)] include an average over the effect of I on D_{12}; we therefore expect a maximum error of ~10% in S_T^d due to the coupling with I_1 and I_2. With regard to the moment of inertia contribution (as discussed in Sec. III C), S_T decreases by ~15% when increasing $d_1 = d_2$ from 0 to 2σ for the $(I_2 = 10m\sigma^2, d_1 = d_2)$ mixtures. Extrapolating this result to the entire range of mass dipoles $d_i \leq 3\sigma$ and moments of inertia, $I_i \leq 260m\sigma^2$, we expect coupling effects in S_T^I of $\lesssim 30\%$ for the mixtures considered in this work.

E. Thermal orientation

The molecules with $d_i \neq 0$ exhibit thermal orientation[49] (TO): they adopt an average orientation with respect to the heat flux vector, quantified by $\langle \cos\theta_i \rangle = \hat{\boldsymbol{u}}_{d,i} \cdot \hat{\boldsymbol{u}}_{J_q}$ for species $i = 1, 2$, where $\hat{\boldsymbol{u}}_{d,i}$ and $\hat{\boldsymbol{u}}_{J_q}$ are the unit vectors in the directions of the mass dipole and heat flux, respectively. Representative $\langle \cos\theta_{z,i} \rangle = \hat{\boldsymbol{u}}_{d,i} \cdot \hat{\boldsymbol{z}}$ profiles from the NEMD simulations are shown in Fig. 11(a). In all cases, $\langle \cos\theta_i \rangle \geq 0$, indicating that on average the mass dipole points toward the cold source (i.e., the heavy side points toward the cold source). This is consistent with simulations of mass-asymmetric diatomic molecules for which the heavier atom preferentially orients toward the cold source[49] and follows the trend in the isotopic Soret effect of binary mixtures where the heavier component migrates toward the cold source (assuming the components are otherwise identical). As shown in Fig. 11(b-i), $\langle \cos\theta_1 \rangle / |\nabla T|$ increases and then begins to saturate with d_1. Holding d_1 constant, $\langle \cos\theta_1 \rangle / |\nabla T|$ increases with decreasing $I = I_1 = I_2$. $\langle \cos\theta_1 \rangle / |\nabla T|$ also depends on d_2 as demonstrated for the $I = 80m\sigma^2$ mixtures; increasing d_2 decreases $\langle \cos\theta_1 \rangle / |\nabla T|$. However, the effects of I and d_2 on $\langle \cos\theta_1 \rangle$ are an order of magnitude smaller than its dependence on d_1.

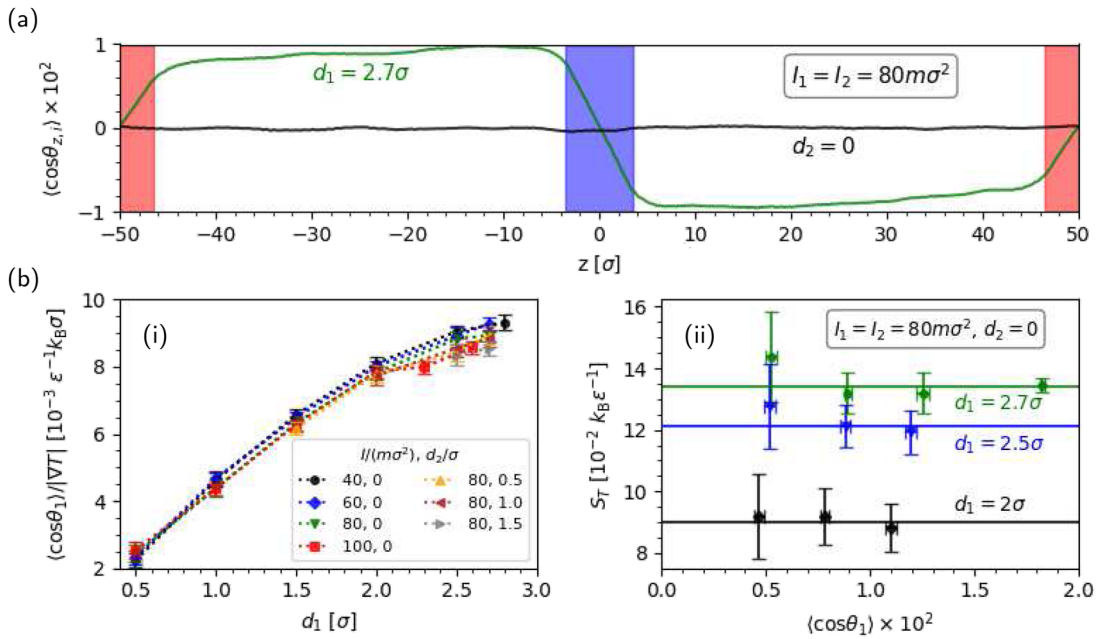

FIG. 11. Thermal orientation of the rod-like molecules. (a) The average orientation $\langle \cos\theta_{z,i} \rangle$ of species $i = 1, 2$ as a function of position z in the NEMD simulations. The blue (cold) and red (hot) indicate the location of the thermostatting regions in the simulation cell. The profiles correspond to the same system shown in Fig. 2. (b) Average orientation $\langle \cos\theta_1 \rangle$ of species 1 for different mixtures: (i) $\langle \cos\theta_1 \rangle / |\nabla T|$ vs the mass dipole d_1 and (ii) the Soret coefficient S_T vs $\langle \cos\theta_1 \rangle$ for different temperature gradients ∇T.

Does thermal orientation have an effect on the Soret coefficient? Based on the general formalism of linear non-equilibrium thermodynamics[32] (LNET), as a coupling effect, it does. For rigid rod-like colloids in the dilute regime, the TO effect decreases $S_T = D_T/D$ primarily by increasing the diffusion coefficient D of the colloid.[25] TO has also been shown to impact the Soret coefficient of Janus particles.[26] However, we show in Fig. 11(b) that for the molecular mixtures studied here the impact of TO is smaller than the uncertainties associated with our S_T data. As exemplified by three different mixtures, S_T does not show a significant dependence on $\langle \cos\theta_i \rangle$. (For each mixture, greater/smaller $|\langle \cos\theta_i \rangle|$ values were achieved by increasing/decreasing ∇T in additional NEMD simulations; see the supplementary material for details). The $|\langle \cos\theta \rangle / \nabla T|$ values observed in this work and in other[49] molecular fluids are ~2–3 orders of magnitude smaller than those observed in the colloidal regime.[24–26] This suggests that TO effects large enough to significantly impact S_T may be more difficult to achieve in molecular mixtures. However, it is worth pointing out that thermal polarization, which emerges from the thermal orientation of polar molecules, can give rise to measurable electrostatic fields in molecular fluids.[50] As a coupling effect, it leads to a reduction in the thermal conductivity of the polar fluid, as described by LNET.[50,51] Thermal polarization can play an important role in determining the thermoelectric response of aqueous solutions.[52] The impact of thermal polarization on the thermal diffusion of polar molecular mixtures remains an open question.

IV. CONCLUSIONS

We have uncovered the mass dipole contribution to the isotopic Soret effect, showing that mixtures of components that differ only by the first moment of their mass distributions can have non-zero Soret coefficients. To the best of our knowledge, all current models of thermal diffusion describe the isotopic contribution S_T^{iso} in terms of only the total mass (the zeroth moment) and moments of inertia (the second moment) of the components. Our results demonstrate that other moments of the mass distribution must be included for a complete description of the (pseudo-)isotopic Soret effect in fluid mixtures.

For the isotopic mixtures of rigid linear molecules examined in this work, the dependence of S_T on the mass dipole arises mainly through the thermal diffusion coefficient D_T. In turn, D_T is correlated with both long-time dynamics—differences in rotational and translational diffusion coefficients, and short-time dynamics—the modification of a librational mode. Regarding the latter, greater mass dipoles give rise to higher frequency librations (of frequency ν_{lib}) with changes of up to 100%, and we find that $D_T \propto \nu_{\mathrm{lib},1} - \nu_{\mathrm{lib},2}$. Through the self-diffusion coefficients $D_{i=1,2}$, the mutual diffusion coefficient D_{12} features a very weak dependence of the mass dipoles, which can be attributed primarily to the effect of d_i on D_i. However, D_{12} does depend significantly on the moment of inertia, which together with $D_T(d_1, d_2)$ affects how S_T varies with the mass dipoles. Indeed, in mixtures with $d_1 \neq d_2$ and $I_1 \neq I_2$, the mass dipole contribution depends on both moments of inertia.

The mass dipole contribution can both enhance or compete with the moment of inertia contribution, giving rise to new phenomenology. For example, it is possible to design isotopic mixtures with $M_1 = M_2$ where the component with a greater moment of inertia is thermophilic. Additionally, the moment of inertia contribution depends on the mass dipoles, even when $d_1 = d_2$ and the mass dipole contribution vanishes. Our results show that changes in the internal mass distribution can be used to tune the Soret coefficient, including its sign and the thermophilicity of the components.

Building on the success of previous empirical models, we show that the mass dipole contribution can be incorporated as an additional additive contribution to the (pseudo-)isotopic Soret effect. This approach is valid when the contributions are only weakly coupled. For the mixtures considered in this work, the weak coupling assumption leads to estimated errors of $\lesssim 10\%$ and $\lesssim 30\%$ for the mass dipole and moment of inertia contributions, respectively. Indeed, the accuracy of the models is limited by the (in)accuracy of the moment of inertia term rather than the weak coupling assumption. Overall, the proposed empirical equations reproduce our simulation data well.

Our work highlights the importance of internal degrees of freedom, such as the mass dipole, in determining the thermodiffusion response of binary mixtures. Further work is required to assess the magnitude of the mass dipole contribution in other molecular mixtures and determine how it affects the phenomenology of these mixtures under the influence of thermal fields.

SUPPLEMENTARY MATERIAL

Supplementary material for this article. (1) Verification of linear response for the Soret coefficients, S_T, calculated from the NEMD simulations. (2) Finite-size analysis of the Soret coefficients. (3) The phenomenological coefficient L_{11}, shear viscosity η, and rotational diffusion coefficient D_r from their Green–Kubo relations. (4) Self-diffusion coefficients from the Einstein relation, related quantities, and finite-size analysis. (5) Estimated isotropic–nematic coexistence conditions. (6) Fitting empirical equations for the thermal diffusion coefficient D_T.

ACKNOWLEDGMENTS

We thank the Leverhulme Trust for Grant No. RPG-2018-384. We gratefully acknowledge a Ph.D. studentship (Project Reference No. 2135626) for O.R.G. sponsored by ICL's Chemistry Doctoral Scholarship Award, funded by the EPSRC Doctoral Training Partnership Account (Grant No. EP/N509486/1). We also acknowledge Imperial College Research Computing Service, http://doi.org/10.14469/hpc/2232.

AUTHOR DECLARATIONS

Conflict of Interest

The authors have no conflicts to disclose.

Author Contributions

Oliver R. Gittus: Conceptualization (lead); Formal analysis (lead); Investigation (lead); Methodology (lead); Writing – original draft

(lead); Writing – review & editing (equal). **Fernando Bresme**: Conceptualization (supporting); Methodology (supporting); Supervision (lead); Writing – original draft (supporting); Writing – review & editing (equal).

DATA AVAILABILITY

The data that support the findings of this study are available from the corresponding author upon reasonable request.

REFERENCES

[1] C. Ludwig, "Diffusion zwischen ungleich erwärmten orten gleich zusammengesetzter lösungen," in *Sitzungsberichte der Bayerischen Akademie der Wissenschaften* (Mathematisch-Naturwissenschaftliche Klasse, 1856), Vol. 539.

[2] C. Soret, "Sur l'état d'équilibre que prend, du point de vue de sa concentration, une dissolution saline primitivement homogène, dont duex parties sort portèes à des temperatures différentes," C. R. Arch. Sci. Phys. Nat., Genève **2**, 48–61 (1879).

[3] R. C. Jones and W. H. Furry, "The separation of isotopes by thermal diffusion," Rev. Mod. Phys. **18**, 151–224 (1946).

[4] S. Chapman, "XIII. The possibility of separating isotopes," London, Edinburgh, Dublin Philos. Mag. J. Sci. **38**, 182–186 (1919).

[5] K. Clusius and G. Dickel, "Neues verfahren zur gasentmischung und isotopentrennung," Naturwissenschaften **26**, 546 (1938).

[6] W. H. Furry, R. C. Jones, and L. Onsager, "On the theory of isotope separation by thermal diffusion," Phys. Rev. **55**, 1083–1095 (1939).

[7] C. Debuschewitz and W. Köhler, "Molecular origin of thermal diffusion in benzene + cyclohexane mixtures," Phys. Rev. Lett. **87**, 055901 (2001).

[8] G. Galliéro, B. Duguay, J.-P. Caltagirone, and F. Montel, "Thermal diffusion sensitivity to the molecular parameters of a binary equimolar mixture, a non-equilibrium molecular dynamics approach," Fluid Phase Equilib. **208**, 171–188 (2003).

[9] P.-A. Artola, B. Rousseau, and G. Galliero, "A new model for thermal diffusion: Kinetic approach," J. Am. Chem. Soc. **130**, 10963–10969 (2008).

[10] D. Reith and F. Müller-Plathe, "On the nature of thermal diffusion in binary Lennard-Jones liquids," J. Chem. Phys. **112**, 2436–2443 (2000).

[11] G. Galliéro, "Thermal diffusion in Lennard–Jones fluids in the frame of the law of the corresponding states," Fluid Phase Equilib. **224**, 13–22 (2004).

[12] H. Hoang and G. Galliero, "Predicting thermodiffusion in simple binary fluid mixtures," Eur. Phys. J. E **45**, 42 (2022).

[13] D. Niether and S. Wiegand, "Thermophoresis of biological and biocompatible compounds in aqueous solution," J. Phys.: Condens. Matter **31**, 503003 (2019).

[14] W. Köhler and K. I. Morozov, "The Soret effect in liquid mixtures—A review," J. Non-Equilib. Thermodyn. **41**, 151–197 (2016).

[15] P.-A. Artola and B. Rousseau, "Thermal diffusion in simple liquid mixtures: What have we learnt from molecular dynamics simulations?," Mol. Phys. **111**, 3394–3403 (2013).

[16] S. Wiegand, "Thermal diffusion in liquid mixtures and polymer solutions," J. Phys.: Condens. Matter **16**, R357–R379 (2004).

[17] G. Wittko and W. Köhler, "Universal isotope effect in thermal diffusion of mixtures containing cyclohexane and cyclohexane-d_{12}," J. Chem. Phys. **123**, 014506 (2005).

[18] B. Pur, W. Köhler, and K. I. Morozov, "The Soret effect of halobenzenes in *n*-alkanes: The pseudo-isotope effect and thermophobicities," J. Chem. Phys. **152**, 054501 (2020).

[19] J. Schirdewahn, A. Klemm, and L. Waldmann, "Thermodiffusion in D_2-HT und anderen wasserstoffgemischen," Z. Naturforsch. A **16**, 133–144 (1961).

[20] W. M. Rutherford, "Effect of mass distribution on the isotopic thermal diffusion of substituted benzenes," J. Chem. Phys. **81**, 6136–6139 (1984).

[21] W. M. Rutherford, "Effect of mass distribution on the isotopic thermal diffusion of benzene," J. Chem. Phys. **86**, 5217 (1987).

[22] W. M. Rutherford, "Isotopic thermal diffusion of carbon disulfide in the liquid phase," J. Chem. Phys. **86**, 397–399 (1987).

[23] W. M. Rutherford, "Effect of carbon and hydrogen isotopic substitutions on the thermal diffusion of benzene," J. Chem. Phys. **90**, 602–603 (1989).

[24] J. Olarte-Plata, J. M. Rubi, and F. Bresme, "Thermophoretic torque in colloidal particles with mass asymmetry," Phys. Rev. E **97**, 052607 (2018).

[25] O. R. Gittus, J. D. Olarte-Plata, and F. Bresme, "Thermal orientation and thermophoresis of anisotropic colloids: The role of the internal composition," Eur. Phys. J. E **42**, 90 (2019).

[26] F. Bresme, J. D. Olarte-Plata, A. Chapman, P. Albella, and C. Green, "Thermophoresis and thermal orientation of Janus nanoparticles in thermal fields," Eur. Phys. J. E **45**, 59 (2022).

[27] T. F. Miller, M. Eleftheriou, P. Pattnaik, A. Ndirango, D. Newns, and G. J. Martyna, "Symplectic quaternion scheme for biophysical molecular dynamics," J. Chem. Phys. **116**, 8649–8659 (2002).

[28] A. P. Thompson, H. M. Aktulga, R. Berger, D. S. Bolintineanu, W. M. Brown, P. S. Crozier, P. J. in't Veld, A. Kohlmeyer, S. G. Moore, T. D. Nguyen, R. Shan, M. J. Stevens, J. Tranchida, C. Trott, and S. J. Plimpton, "LAMMPS—A flexible simulation tool for particle-based materials modeling at the atomic, meso, and continuum scales," Comput. Phys. Commun. **271**, 108171 (2022).

[29] C. D. Daub, P.-O. Åstrand, and F. Bresme, "Thermo-molecular orientation effects in fluids of dipolar dumbbells," Phys. Chem. Chem. Phys. **16**, 22097–22106 (2014).

[30] J. E. Basconi and M. R. Shirts, "Effects of temperature control algorithms on transport properties and kinetics in molecular dynamics simulations," J. Chem. Theory Comput. **9**, 2887–2899 (2013).

[31] A. Kowaguchi, P. E. Brumby, and K. Yasuoka, "Phase transitions and hysteresis for a simple model liquid crystal by replica-exchange Monte Carlo simulations," Molecules **26**, 1421 (2021).

[32] S. R. de Groot and P. Mazur, *Non-Equilibrium Thermodynamics* (Dover, 1984).

[33] O. R. Gittus and F. Bresme, "On the microscopic origin of Soret coefficient minima in liquid mixtures," Phys. Chem. Chem. Phys. **25**, 1606–1611 (2023).

[34] A. Perronace, G. Ciccotti, F. Leroy, A. H. Fuchs, and B. Rousseau, "Soret coefficient for liquid argon-krypton mixtures via equilibrium and nonequilibrium molecular dynamics: A comparison with experiments," Phys. Rev. E **66**, 031201 (2002).

[35] N. A. T. Miller, P. J. Daivis, I. K. Snook, and B. D. Todd, "Computation of thermodynamic and transport properties to predict thermophoretic effects in an argon-krypton mixture," J. Chem. Phys. **139**, 144504 (2013).

[36] D. Surblys, H. Matsubara, G. Kikugawa, and T. Ohara, "Application of atomic stress to compute heat flux via molecular dynamics for systems with many-body interactions," Phys. Rev. E **99**, 051301 (2019).

[37] D. Surblys, H. Matsubara, G. Kikugawa, and T. Ohara, "Methodology and meaning of computing heat flux via atomic stress in systems with constraint dynamics," J. Appl. Phys. **130**, 215104 (2021).

[38] Due to an implementation detail in LAMMPS the *y* and *z* components of the heat flux for rigid bodies are highly unphysical and should not be used.

[39] LAMMPS Development Team, LAMMPS documentation, https://docs.lammps.org/compute_heat_flux.html (accessed 1 July 2022).

[40] D. J. Evans and S. Murad, "Thermal conductivity in molecular fluids," Mol. Phys. **68**, 1219–1223 (1989).

[41] I.-C. Yeh and G. Hummer, "System-size dependence of diffusion coefficients and viscosities from molecular dynamics simulations with periodic boundary conditions," J. Phys. Chem. B **108**, 15873–15879 (2004).

[42] S. H. Jamali, L. Wolff, T. M. Becker, A. Bardow, T. J. H. Vlugt, and O. A. Moultos, "Finite-size effects of binary mutual diffusion coefficients from molecular dynamics," J. Chem. Theory Comput. **14**, 2667–2677 (2018).

[43] M. Eslamian and M. Z. Saghir, "A critical review of thermodiffusion models: Role and significance of the heat of transport and the activation energy of viscous flow," J. Non-Equilib. Thermodyn. **34**, 97–131 (2009).

[44] D. M. Heyes, "Translational and rotational diffusion of rod shaped molecules by molecular dynamics simulations," J. Chem. Phys. **150**, 184503 (2019).

[45] M. Doi and S. F. Edwards, *The Theory of Polymer Dynamics* (Clarendon Press, 1986).

[46]J. M. Kincaid, E. G. D. Cohen, and M. López de Haro, "The Enskog theory for multicomponent mixtures. IV. Thermal diffusion," J. Chem. Phys. **86**, 963–975 (1987).
[47]S. Villain-Guillot and A. Würger, "Thermal diffusion in a binary liquid due to rectified molecular fluctuations," Phys. Rev. E **83**, 030501 (2011).
[48]S. Hartmann, W. Köhler, and K. I. Morozov, "The isotope Soret effect in molecular liquids: A quantum effect at room temperatures," Soft Matter **8**, 1355–1360 (2012).
[49]F. Römer, F. Bresme, J. Muscatello, D. Bedeaux, and J. M. Rubí, "Thermomolecular orientation of nonpolar fluids," Phys. Rev. Lett. **108**, 105901 (2012).
[50]O. R. Gittus, P. Albella, and F. Bresme, "Polarization of acetonitrile under thermal fields via non-equilibrium molecular dynamics simulations," J. Chem. Phys. **153**, 204503 (2020).
[51]F. Bresme, A. Lervik, D. Bedeaux, and S. Kjelstrup, "Water polarization under thermal gradients," Phys. Rev. Lett. **101**, 020602 (2008).
[52]S. Di Lecce and F. Bresme, "Thermal polarization of water influences the thermoelectric response of aqueous solutions," J. Phys. Chem. B **122**, 1662–1668 (2018).
[53]J. D. Weeks, D. Chandler, and H. C. Andersen, J. Chem. Phys. **54**, 5237–5247 (1971).